

Article

Direct Femtosecond Laser Processing for Generating High Spatial Frequency LIPSS (HSFL) on Borosilicate Glasses with Large-Area Coverage

Rajeev Rajendran ¹ , E. R. Krishnadev ¹ and K. K. Anoop ^{1,2,*} 

¹ Department of Physics, Cochin University of Science and Technology, Kochi-22, Cochin 682022, Kerala, India; rajeevrajendran@cusat.ac.in (R.R.); krishnadevramachandran@gmail.com (E.R.K.)

² Inter University Centre for Nanomaterials and Devices (IUCND), Cochin University of Science and Technology, Cochin 682022, Kerala, India

* Correspondence: anoopkk@cusat.ac.in

Abstract: Large-area nanostructuring of glasses using intense laser beams is a challenging task due to the material's extreme non-linear absorption of laser energy. Precise optimization of the process parameters is essential for fabricating nanostructures with large-area coverage. In this study, we report the findings on creating high-spatial-frequency LIPSS (HSFL) on borosilicate glass through direct laser writing, using a femtosecond laser with a wavelength $\lambda = 800$ nm, pulse duration $\tau = 35$ fs, and repetition frequency $f_{rep} = 1$ kHz. We measured the single-pulse ablation threshold and incubation factor of Borosilicate glasses to achieve high-precision control of the large-area surface structuring. Single-spot experiments indicated that, when there was higher fluence and a larger number of irradiated laser pulses, a melt formation inside the irradiated area limited the uniformity of LIPSS formation. Additionally, the orientation of the scan axis with the laser beam polarization was found to significantly influence the uniformity of LIPSS generated along the scan line, with more redeposition and melt formation when the scan axis was perpendicular to the laser beam polarization. For large-area processing, the borosilicate glass surface was scanned line-by-line by the laser beam, with a scan orientation parallel to the polarization of the laser. The optical characterization revealed that the transmittance and reflectance of the borosilicate glass decreased significantly after processing. Additionally, the surface's wettability changed from hydrophilic to super-hydrophilic after processing. These chemical contamination-free and uniformly distributed structures have potential applications in optics, microfluidics, photovoltaics, and biomaterials.

Keywords: femtosecond laser processing; laser-induced periodic surface structures (LIPSS); high-spatial-frequency LIPSS (HSFL); borosilicate glass



Citation: Rajendran, R.; Krishnadev, E.R.; Anoop, K.K. Direct Femtosecond Laser Processing for Generating High Spatial Frequency LIPSS (HSFL) on Borosilicate Glasses with Large-Area Coverage. *Photonics* **2023**, *10*, 793. <https://doi.org/10.3390/photonics10070793>

Received: 24 May 2023

Revised: 23 June 2023

Accepted: 27 June 2023

Published: 10 July 2023



Copyright: © 2023 by the authors. Licensee MDPI, Basel, Switzerland. This article is an open access article distributed under the terms and conditions of the Creative Commons Attribution (CC BY) license (<https://creativecommons.org/licenses/by/4.0/>).

1. Introduction

For the past few decades, the generation of laser-induced periodic surface structures (LIPSS) on various materials has been studied extensively due to its vast applications in optoelectronics, photonics, plasmonics, biomaterials and thermal radiation sources [1–5]. LIPSS can be generated on any solid material by irradiating the material surface with any linearly polarized laser light that has a fluence near the ablation threshold of the material [6]. Ultrashort pulsed lasers are efficient at generating LIPSS on nearly all kinds of solid materials [2,7]. It can create LIPSS on metals, semiconductors and dielectrics [8–11]. Based on the spatial periodicity of the induced structures, LIPSS can be categorized into two main divisions: low-spatial-frequency LIPSS (LSFL) and high-spatial-frequency LIPSS (HSFL). LSFLs have a periodicity close to the laser wavelength λ ($\Lambda_{LSFL} > \lambda/2$), and HSFL have a periodicity less than half of the laser wavelength λ ($\Lambda_{HSFL} < \lambda/2$) [12]. The formation of LSFL is thought to be caused by the interference of the incident laser beam with surface electromagnetic waves (SEWs) [13,14] and/or surface plasmon polaritons (SPPs) [7,15,16].

The formation of high-spatial-frequency LIPSS (HSFL) has been debated, with various theories suggesting self-organization [14], nanoplasmonic excitations [17,18], interference, second-harmonic generation [19–21] and Marangoni bursting [22], etc. The self-organization of nanoplasmas is believed to occur due to their semi-metallic properties, which affect the propagation of fields in a manner similar to planar metallic waveguides. The growth of planes is favored if they support modes whose field distribution reinforces their own growth, or where the field is enhanced by a suitably placed neighbor. The spacing between the planes is determined solely by the mode structure and scales linearly with the wavelength, independent of the laser pulse energy [23]. According to the theory of nanoplasmonics, when the pulse fluence reaches the ablation threshold, a pair of peripheral nanoplasma zones are created. These zones lead to local intensity enhancement, which can cause formation of more nanoplasma zones. This process, known as self-seeding, can lead to the formation of the periodic structure [17]. The interference effect is also a significant mechanism that predicts HSFL formation. Multi-photon absorption produces electrically unstable surfaces that result in intense emission of electrons and positive ions, which then form surface plasma and plasmons [24]. Surface plasmons are excited and interfere with absorbed laser field. This strongly reprofiles the intensity, creating periodic patterns that locally enhance the field and ablation that leads to the formation of periodic structures [25]. As the ripples grow, the grating-assisted surface-plasmon laser coupling plays an important role in further process [26]. Additionally, compound materials are anticipated to undergo modifications during multi-pulse irradiation. Thus, the near-surface region of these materials might facilitate harmonic generation and explain an orientation-insensitivity. It has been approximated that some of HSFL periods are laser second-harmonic wavelengths [27]. Besides these, Zhang et al. proposed that Marangoni bursting can be the primary driving force for the generation of HSFL when a transition metal placed in an organic solvent is irradiated by a femtosecond laser [22].

The spatial periodicity of the LIPSS under the irradiation with femtosecond laser pulses has been found to depend upon various experimental parameters, including incident laser wavelength [28,29], laser fluence [30], polarization [31], number of pulses [15], the ambient environment [32,33], and the properties of the material [34]. Taher et al. reported that the spatial periodicity of LSFL varied from $\lambda/1.7$ to $\lambda/4.7$ and HSFL altered from $\lambda/8$ to $\lambda/30$ upon increasing the wavelength from 400 nm to 2200 nm [28]. Shi et al. reported that lower fluence corresponds to the generation of HSFL and higher fluence corresponds to the generation of LSFL [30]. Bonse et al. showed that at a fixed peak fluence, the mean spatial periodicity of LIPSS generated on single crystalline silicon decreases monotonously between 770 nm and 560 nm as the number of shots increases from 1 to 1000 [15]. Gregorčič et al. reported that the rotation in the polarization of the irradiated picosecond laser pulse resulted in a corresponding rotation in the ripples produced on a steel substrate [31]. Gräf et al. reported that the threshold fluence for the formation of LSFL on fused silica is reduced and the periodicity of LSFL is increased by increasing the substrate temperature [32]. Nürnberger et al. reported that the orientation of LIPSS generated is influenced by the grain structure and the crystal orientation of each individual grain of the substrate [34].

The superior mechanical, physical, and chemical characteristics of the materials, such as borosilicate glass, soda–lime glass, and fused silica, make them into ideal choices for applications in optics, microfluidics, photovoltaics, and biomaterials [35]. Femtosecond laser-assisted processing has become a powerful and efficient way to nano-/microfabricate glass surfaces [36]. Many works have reported the formation of LIPSS on glass [13,37]. However, most of them are limited to a single spot or line segment. The lack of investigations is due to difficulties with LIPSS generation on glasses that are mostly brought on by the amorphous chemical structure and comparatively high band-gap energy of glass when compared to metals and semiconductors. This high band-gap energy causes ultrashort laser pulses to undergo non-linear, multi-photon absorption. These properties make glasses more vulnerable to changes in laser irradiation, defects, and incubation [35]. Additionally, only

several studies exist that reported on generating LIPSS on borosilicate glass when compared to other glasses. LSFL are typically formed for higher laser fluences or number of pulses on silica-based glasses [13,37–39]. HSFL were observed only in few glasses [13,40]. Höhm et al. has reported the generation of high-spatial-frequency LIPSS, with spatial periods between 170 nm and 450 nm and an orientation perpendicular to the polarization on silica, using a femtosecond laser with a central wavelength of 800 nm and a pulse duration 150 fs [13]. This work study aims to explore the potential for creating high-spatial-frequency LIPSS (HSFL) over a large surface area of borosilicate glass. Additionally, we studied the optical and wetting characteristics of the induced structures.

2. Materials and Methods

Surface texturing of borosilicate glass was conducted by irradiating with a Ti-sapphire femtosecond laser system (Coherent Astrella) that emits a linearly polarized laser pulse of energy 7 mJ for a pulse duration of 35 fs. The laser has a central wavelength of 800 nm and a repetition rate of 1 kHz. An electromechanical shutter is used to control the laser dose applied to the target. A combination of half-wave plate and polarizing beamsplitter was used in the optical path to precisely control laser energy and choose a particular polarization. The beam was focused using a lens of 300 mm focal length onto the surface of the sample at normal incidence. Optically flat borosilicate glass of thickness 130 μm was used as the substrate. This was mounted onto a motorized XY translation stage for line-by-line scanning. All the texturing processes were carried out in atmospheric conditions and the complete schematic is shown in Figure 1.

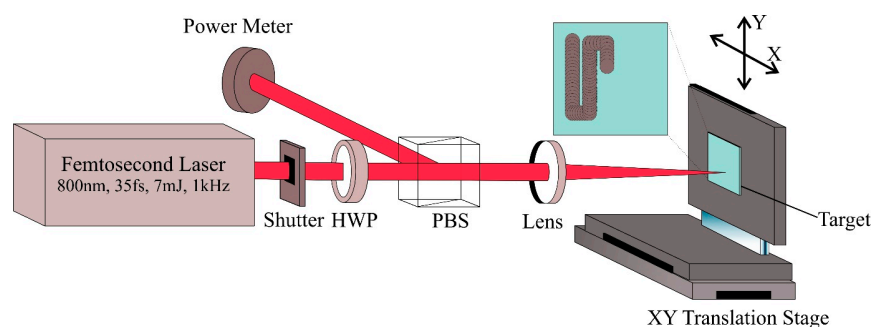


Figure 1. Schematic of the experimental setup used for femtosecond laser processing. HWP: half waveplate, PBS: polarizing cube beamsplitter.

The ablation threshold for a different number of laser pulses was determined using the D square method or Liu’s method [41], and the incubation parameter was determined using the accumulation model designed by Jee et al. [42]. For this, the surface of the substrate was irradiated with different number of shots ranging from 10 to 100, with different pulse energies ranging from 20 μJ to 100 μJ . The generation of LIPSS upon the variation in pulse number and pulse energy was studied by analyzing the topography of the crater formed on the substrate. Additionally, the generation of LIPSS over a single line was investigated for scanning orientation parallel and perpendicular to the laser beam polarization by varying the scanning speed. The large-area structuring was performed by line-by-line scanning over an area of $5 \times 5 \text{ mm}^2$, with a peak laser fluence of 2.71 J/cm^2 at a scanning speed of $2000 \mu\text{m/s}$ along a scanning orientation parallel to the polarization axis.

The topographical analysis of the processed substrate surface was conducted using a field emission scanning electron microscope (Carl Zeiss Sigma VP) and an atomic force microscope (Keysight 5500AM). Additionally, the reflectance and transmittance of the processed substrate surface was determined using a UV-visible, near-IR spectrophotometer (Jasco V770). The wetting properties of the processed substrate surface were analyzed using a contact angle goniometer (Rame-hart 290-U1).

The quantitative analysis of the LIPSS generated on the material surface was conducted using the opensource software Gwyddion 2.62 [43] and imageJ 1.53k [44]. The

two-dimensional fast Fourier transform (2D FFT) of the FESEM images was generated and analyzed using Gwyddion software. The analysis of the dispersion of the LIPSS orientation angle (DLOA) [45] was conducted using the plugin OrientationJ [46] (orientation distribution module with Riesz filters) of ImageJ software. To compare the DLOA for different processing conditions, we used a constant area of $9 \times 9 \mu\text{m}^2$ of the FESEM images, taken under the same acquisition conditions, with a magnification of $20,000\times$.

3. Results and Discussion

3.1. Ablation Threshold Estimation

The ablation threshold of borosilicate glass was estimated using the D -squared method introduced by Liu [41]. According to this method, the diameter of the ablation crater is related to the applied laser pulse energy through the equation,

$$D^2 = 2\omega_0^2 \ln\left(\frac{E}{E_{th}}\right) \tag{1}$$

where D is the crater diameter, ω_0 is the Gaussian beam radius at $1/e^2$ the peak value, E is the laser pulse energy and E_{th} is threshold pulse energy. For a Gaussian laser profile, threshold peak fluence (F_{th}) can be related to the threshold pulse energy (E_{th}) by

$$F_{th} = \frac{2E_{th}}{\pi\omega_0^2} \tag{2}$$

The diameter of the crater was estimated accurately from the FESEM images. The beam radius was estimated by plotting the square of the crater diameters (D^2) versus the logarithm of the laser pulse energy (E) for different numbers of irradiated laser pulses, as shown in Figure 2a, and the value was found to be $27.12 \pm 1.95 \mu\text{m}$. By extrapolating the least-squares fit curve, the threshold pulse energy and threshold fluence for different numbers of laser pulses were estimated.

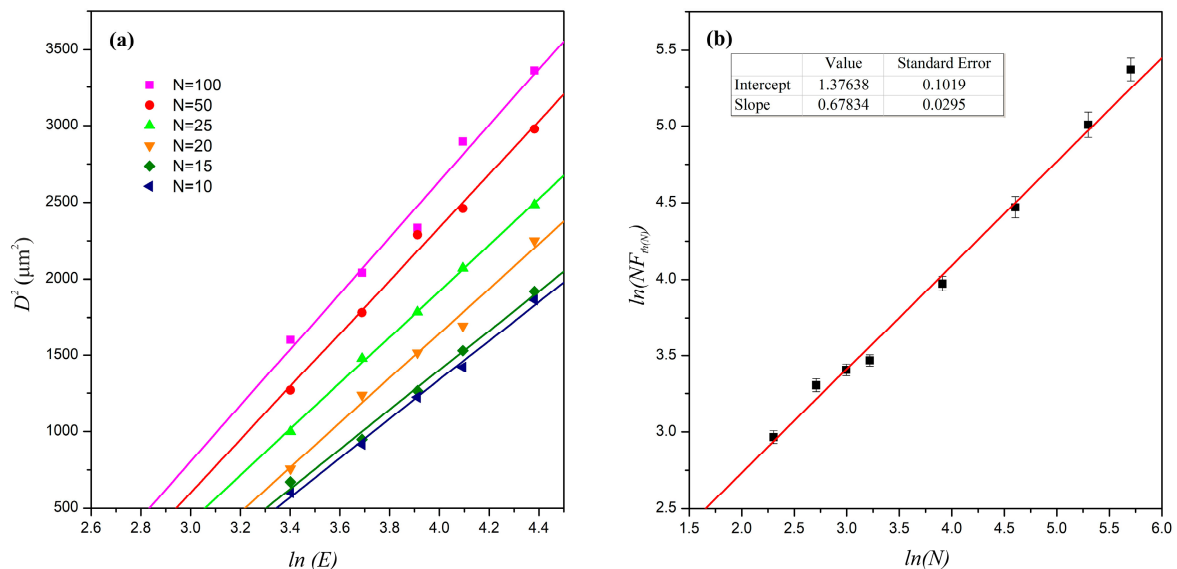


Figure 2. (a) The squared diameter, D^2 , of the ablated craters is plotted as a function of the logarithm of laser pulse energy for different number of laser pulses. The solid lines represent the least-squares fit according to Equation (1). (b) Logarithm of the product of the number of laser pulses and the corresponding threshold fluence plotted as a function of logarithm of number of laser pulses and the solid line represent the least-squares fit according to Equation (3).

The ablation threshold decreased from 1.94 J/cm² to 0.87 J/cm² when the number of laser pulses increased from 10 to 100 shots. This was caused by the material-dependent “incubation effect” [47–49]. The incubation effect is attributed due to the generation of surface defects by the interaction of multiple laser pulses with fluences lower than the single-shot ablation threshold. These defects can cause ablation at lower threshold levels as they alter the mechanical and/or chemical properties of the material [50,51]. In the case of femtosecond laser ablation, the most likely hypothesis on the origin of incubation is an increment in surface roughness after multi-shot irradiation due to ripple formation or the accumulation of surface defects. The initial laser pulses cause imperfections in the material, allowing subsequent pulses to be absorbed better, and thus improving the ablation and material removal process [52].

The observed accumulation behavior has been explained in terms of an incubation model by Jee et al. [42]. The ablation threshold fluence $F_{th(N)}$ for N laser shots is related to the single-shot ablation threshold fluence through the power law:

$$F_{th(N)} = F_{th(1)} N^{S-1} \quad (3)$$

The incubation coefficient S (usually less than 1) serves to quantify the degree of accumulation that is present in a material. When S equals 1, the effect of accumulation is null, and the ablation threshold will be a constant value irrespective of the number of incident laser pulses. It can be understood from Equation (3) that the logarithm of the product $N F_{th(N)}$ is proportional to $\ln N$, with the proportionality constant S . In Figure 2b, the slope of the plot, which is the incubation parameter, is $S = 0.68 \pm 0.03$. This S value determines that there is a significant accumulation effect present in the femtosecond laser processing of the material. By using Equation (3) and the incubation parameter S , the single-shot ablation threshold was found to be $F_{th(1)} = 3.87 \pm 0.26$ J/cm². Gräf et al. reported an ablation threshold of 4.1 J/cm² for borosilicate glass upon undergoing irradiation with 5 shots of femtosecond laser pulse with a pulse duration of 300 fs and a central wavelength 1025 nm [39].

3.2. Single Spot Analysis

The evolution of LIPSS on borosilicate glass at a single spot was analyzed by varying the number of shots and the fluence of the incident laser light. The FESEM image of the crater that formed on the borosilicate glass irradiated with different numbers of linearly polarized femtosecond laser pulses at different peak fluences is shown in Figure 3. The laser peak fluence varied from 2.27 J/cm² to 6.80 J/cm² and the number of pulses also varied from 10 to 50. It was observed that laser-induced periodic surface structures (LIPSS), having an orientation parallel to the electric field vector, were formed on the borosilicate glass surface when it was irradiated with femtosecond laser pulses in the investigated parametric range. When the number of irradiated laser pulses was increased by keeping the laser peak fluence at a fixed value, e.g., $F = 2.27$ J/cm² (Figure 3a,e,i,m,q), the peripheral region of the crater was found to be losing its periodic nature, leading to the formation of random nano-/microstructures over the outer region of crater. Additionally, on increasing the irradiated laser peak fluence for a fixed number of shots, e.g., 10 shots (Figure 3a–d), a melt formation was observed at the central region of the crater where the intensity was the maximum for a Gaussian beam profile and LIPSS formation was limited to the peripheral region of the crater. Gräf et al. and Ben-Yakar et al. reported the melt formation at the center of the crater of borosilicate glass at higher laser peak fluences [39,53].

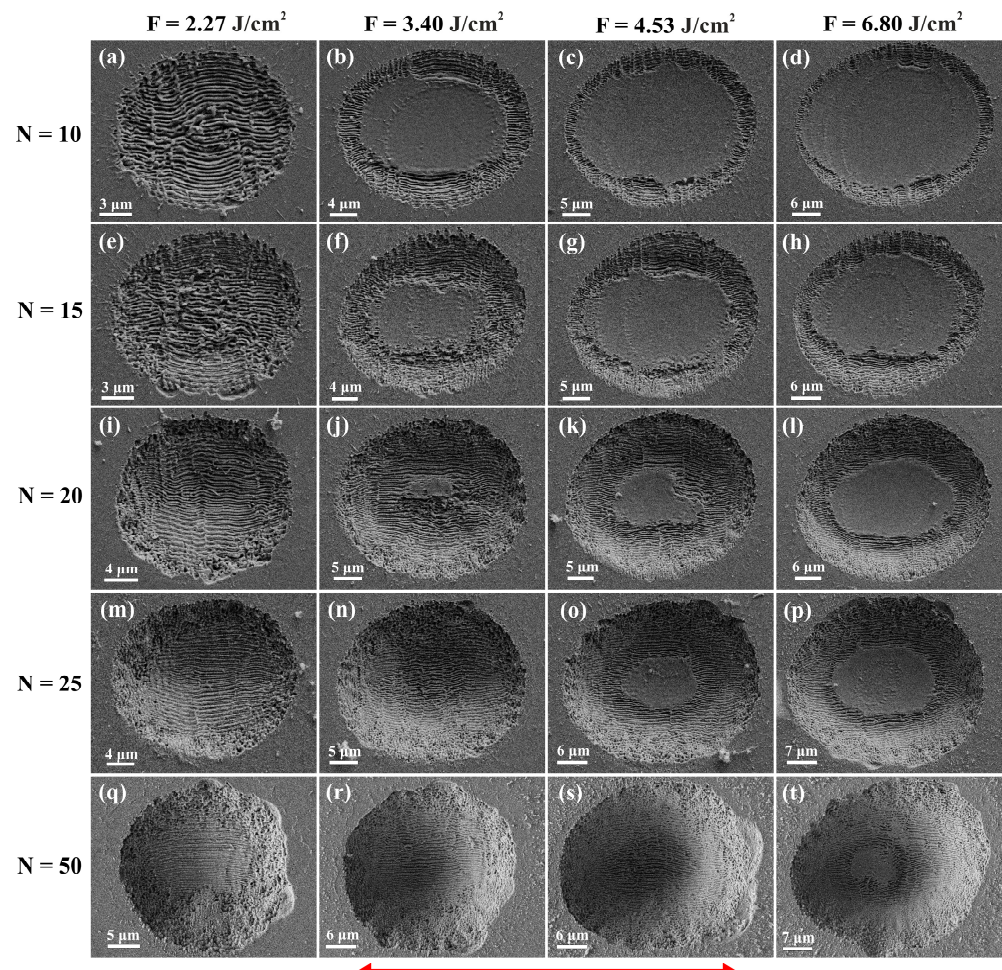


Figure 3. (a–t) FESEM images of the craters on the surface of borosilicate glass generated upon irradiation with different number of laser pulses, N , at varying peak fluences, F . The rows correspond to different number of laser pulses and the columns correspond to different fluences. The red arrow indicates the direction of the electric field vector.

When a substrate is irradiated with ultrashort laser pulses, a major portion of the absorbed energy by the substrate will be utilized by the plasma to expand into its surrounding gas [54]. A small portion of it remains in the substrate as thermal energy. This thermal energy, deposited in the bulk of the glass, forms a transient shallow area of molten glass beneath the expanding plasma [55]. During the lifespan of the melt, the forces (thermocapillary forces and the forces by the plasma pressure) acting on the molten material drive the liquid to the crater’s edges. When the melt resolidifies, they produce a raised rim around the ablated crater [53]. According to Gräf et al., these melt formations are unaffected by the inter-pulse effect of heat accumulation due to the sequential irradiation of laser pulses [39]. However, in our studies, we found that the size of these melt formations is reduced and even totally removed on increasing the number of shots (Figure 3n,r,s).

A quantitative analysis of the melt zone is conducted by taking the ratio of the melt zone to the crater area as a function of laser fluence and incident number of laser pulses as shown in Figure 4. The heat map representation is such that the darker region indicates more melt zone formation. According to this heat map, the most favorable conditions for the generation of a crater without melt zone is indicated by the lightly colored region.

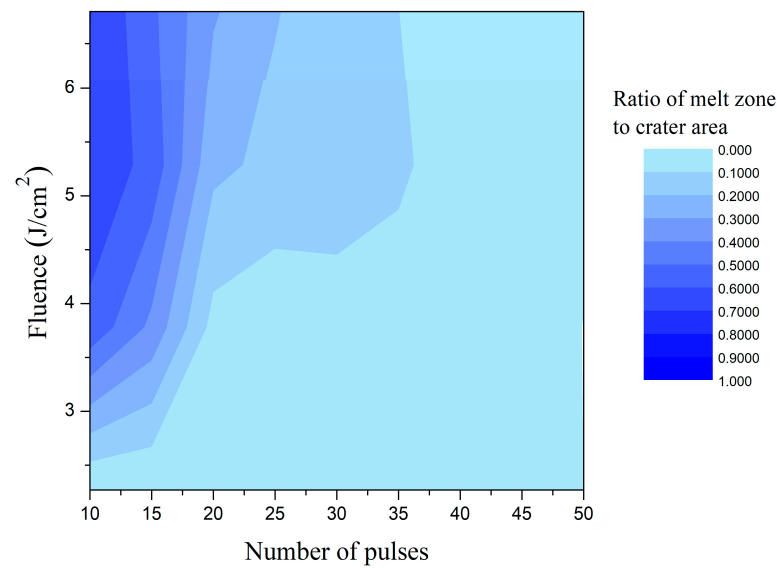


Figure 4. Heat map of the ratio of melt zone to crater area as a function of fluence and number of pulses.

Upon observing the topography of a crater formed by irradiating the substrate with 20 laser pulses with a fluence of 2.27 J/cm^2 (Figure 5), it was found that the crater is fully covered with LIPSS. The 2D fast Fourier transform of the FESEM image of the crater (Figure 5c) reveals that the crater is covered mostly with LIPSS of periodicity $573 \pm 46 \text{ nm}$, $307 \pm 19 \text{ nm}$ and $195 \pm 15 \text{ nm}$. Where the ripples with periodicity of $573 \pm 46 \text{ nm}$ are categorized as low-spatial-frequency LIPSS (LSFL) and ripples with periodicities of $307 \pm 19 \text{ nm}$ and $195 \pm 15 \text{ nm}$ are categorized as high-spatial-frequency LIPSS (HSFL) [12].

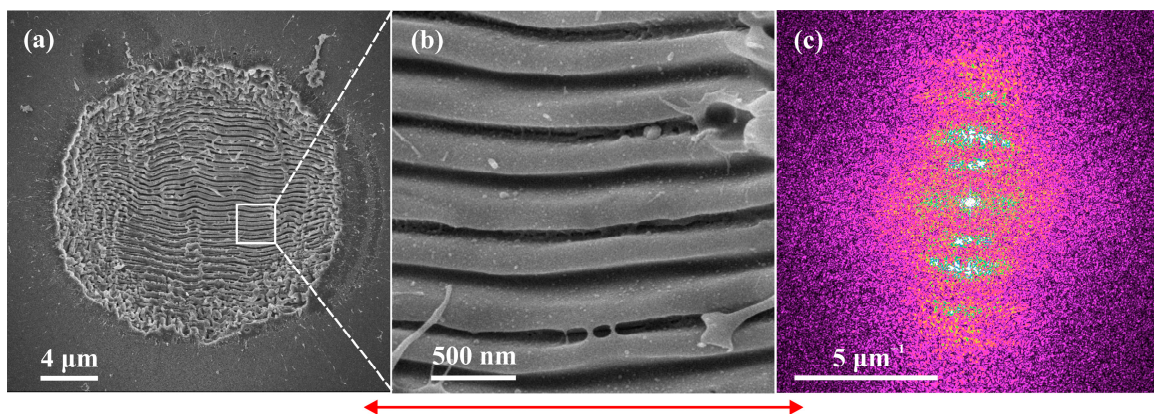


Figure 5. (a) FESEM image of a crater formed by irradiating the substrate with 20 laser pulses having a fluence of 2.27 J/cm^2 , (b) magnified image of the LIPSS and (c) 2D fast Fourier transform (FFT) of the FESEM image of crater shown in (a). The red arrow indicates the direction of the electric field vector.

3.3. Large-Area HSFL

Based on the single-spot trials, further investigations were performed to realize large-area homogenous structuring with high-spatial-frequency LIPSS (HSFL). For the generation of HSFL over a large area, LIPSS formation behavior in a single scan line parallel and perpendicular to the axis of the electric field vector was studied. For this, the surface of the substrate was irradiated in a scanning manner with a laser peak fluence of 2.71 J/cm^2 at different scanning speeds, $1000 \mu\text{m/s}$, $1500 \mu\text{m/s}$ and $2000 \mu\text{m/s}$, along the horizontal and vertical scanning directions. Since the beam diameter was $\sim 54 \mu\text{m}$, the effective number of laser pulse per beam diameter was 54, 36 and 27, respectively. This fluence and the effective

number of pulses fall within the lightly colored favorable region of the heat map shown in Figure 4.

The ripple structures generated on the material surface were analyzed qualitatively and quantitatively. The qualitative analysis revealed that, at a lower scan speed of $1000 \mu\text{m/s}$ (Figure 6a,d), the redeposition of nanoparticles was high when compared to that of higher scan speeds. When comparing the structures according to the scanning orientation, scanning along the vertical axis (\perp to the direction of the electric field vector) found it to have more redeposition than scanning along the horizontal direction (\parallel to the direction of the electric field vector). Additionally, the melt formations were observed at a higher scanning speed of $2000 \mu\text{m/s}$ along the vertical direction (Figure 6f). So, it is clear that the orientation of the scan axis with the laser beam polarization significantly affects the uniformity of large-area processing, with redeposition and melt formation being higher when the scan axis is perpendicular to the laser beam polarization.

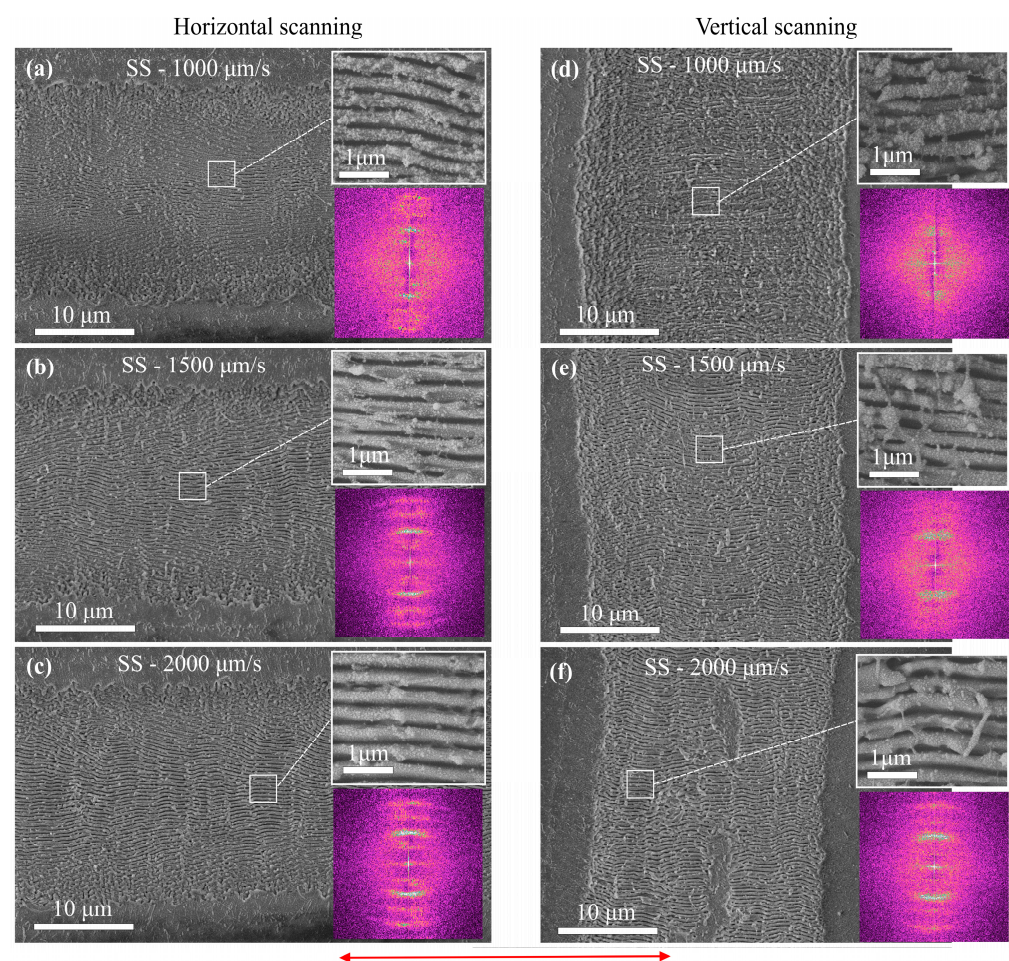


Figure 6. FESEM images of the surface of borosilicate glass upon scanning with different scanning speed (SS) along horizontal (a–c) and vertical (d–f) direction with a laser peak fluence of 2.71 J/cm^2 . The magnified image of HSFL and the 2D FFT of the FESEM image are shown in the inset of each image. The 2D FFT image size is $10 \mu\text{m}^{-1} \times 10 \mu\text{m}^{-1}$. The red arrow indicates the direction of the electric field vector.

The ripple structures were quantitatively analyzed by taking the fast Fourier transform of the FESEM images (inset image of Figure 6). In the FFT images, the most prominent ripple structure has a periodicity of approximately 360 nm . Additionally, the density of this ripple structure increases as the scanning speed increases. The regularity of the periodic structures was characterized by analyzing the dispersion of the LIPSS orientation angle (DLOA). The DLOA is defined as the half-width at half-maximum value of the distribution

in the FFT. The analysis was conducted for an area of $9 \times 9 \mu\text{m}^2$ of the FESEM images. The normalized data of LIPSS orientation (Figure 7a,b) reveals that the distribution is centered around 0° , which implies that the LIPSS orientation is mostly parallel to the electric field vector. For highly regular structures, dispersion angles of the orientation are very low. So, from Figure 7c, it is clear that the only favorable scan speeds are $2000 \mu\text{m/s}$ for vertical scanning and $1500 \mu\text{m/s}$ and $2000 \mu\text{m/s}$ for horizontal scanning. However, from a qualitative standpoint, vertical scanning with a scan speed of $2000 \mu\text{m/s}$ is not preferable due to the melt zone formation. Additionally, horizontal scanning with a scan speed of $1500 \mu\text{m/s}$ is not preferable due to increased nanoparticle redeposition. Therefore, horizontal scanning with a scan speed of $2000 \mu\text{m/s}$ is the preferable option for the large-area processing.

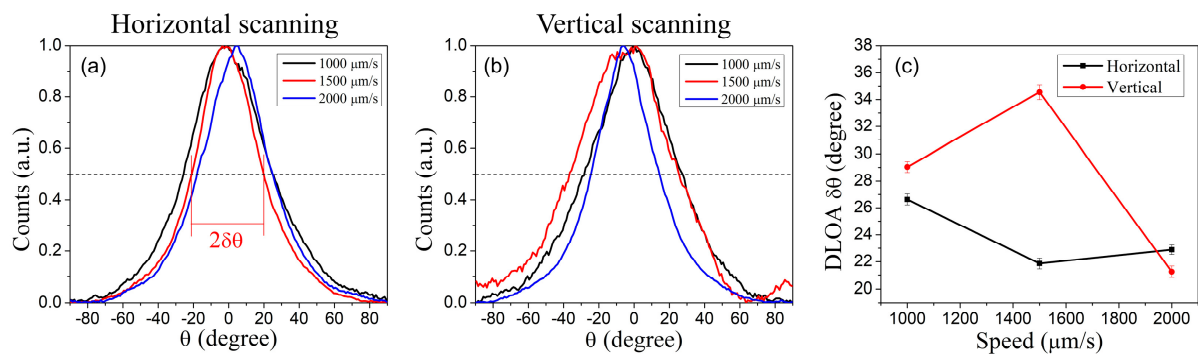


Figure 7. Dispersion of the LIPSS orientation angle (DLOA) for (a) horizontal scanning and (b) vertical scanning. (c) DLOA value as a function of scanning speed for horizontal and vertical scanning.

The large-area HSFL on borosilicate glass was generated by line-by-line scanning over the glass surface at a scan speed of $2000 \mu\text{m/s}$ along the horizontal direction with a laser peak fluence of 2.71 J/cm^2 . Since the single-line analysis revealed the width of the ablated area to be $\sim 22 \mu\text{m}$, the spacing between the lines was fixed at $\Delta x = 22 \mu\text{m}$. The macroscopic image of the femtosecond laser processed borosilicate glass shown in Figure 8a reveals that the surface exhibits iridescence due to the presence of uniform HSFL. The FESEM image of the HSFL, generated on borosilicate glass, the magnified image of the central area of the scan line, and the overlapping area of the two-scan line are also shown in Figure 8b–d. The interface of the two lines is observed as losing its periodicity and this is due to the incubation effect. The 2D fast Fourier transform (FFT) (Figure 8e) of the large area shows that the periodicity of the HSFL is $\sim 380 \text{ nm}$. Additionally, the AFM measurements (Figure 8f) reveal that the depth of the grooves are $\sim 130 \text{ nm}$.

The transmittance and total reflectance of the surface-structured borosilicate glass were measured and compared with those of unstructured borosilicate glass. As shown in Figure 9a,b the transmittance and the reflectance of the glass surface were significantly reduced after HSFL formation. This may be due to the scattering or absorption by the micro/nanostructures, the light trapping capability of the regular periodic nanostructures and degradation of a material's property by laser irradiation [37,56,57]. The low reflectivity of the material surface's can be attributed to the anti-reflective properties of the periodic structures, which have been discussed in multiple investigations [56–59]. The reduction in the transmission can be attributed to the crystal formation at the surface of the glass, which alters the absorption characteristics of the incident radiation [60].

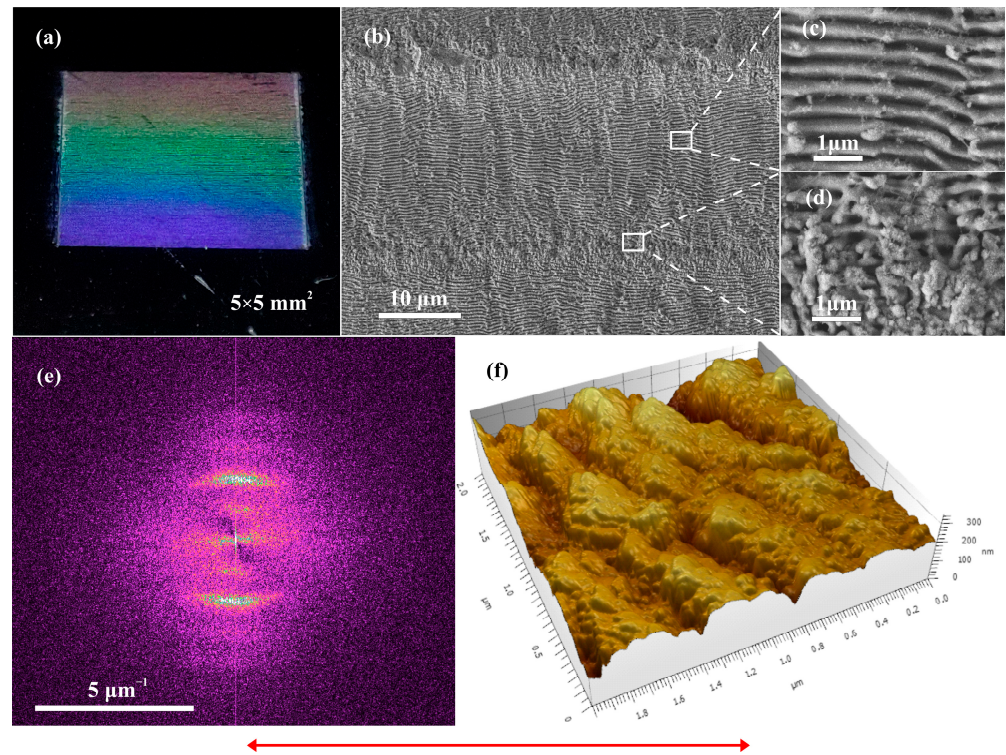


Figure 8. (a) Macroscopic image of the processed borosilicate glass surface with uniform HSFL. (b–d) FESEM images of the large-area HSFL on a borosilicate glass surface upon irradiating the surface with a laser peak fluence of 2.71 J/cm^2 at a scanning speed of $2000 \text{ } \mu\text{m/s}$ along horizontal direction with a line spacing of $\Delta x = 22 \text{ } \mu\text{m}$. The magnified images are shown inset. (e) 2D fast Fourier transform (FFT) of the large area shown in (b). (f) 3D AFM image of the HSFL on borosilicate glass. The red arrow indicates the direction of the electric field vector.

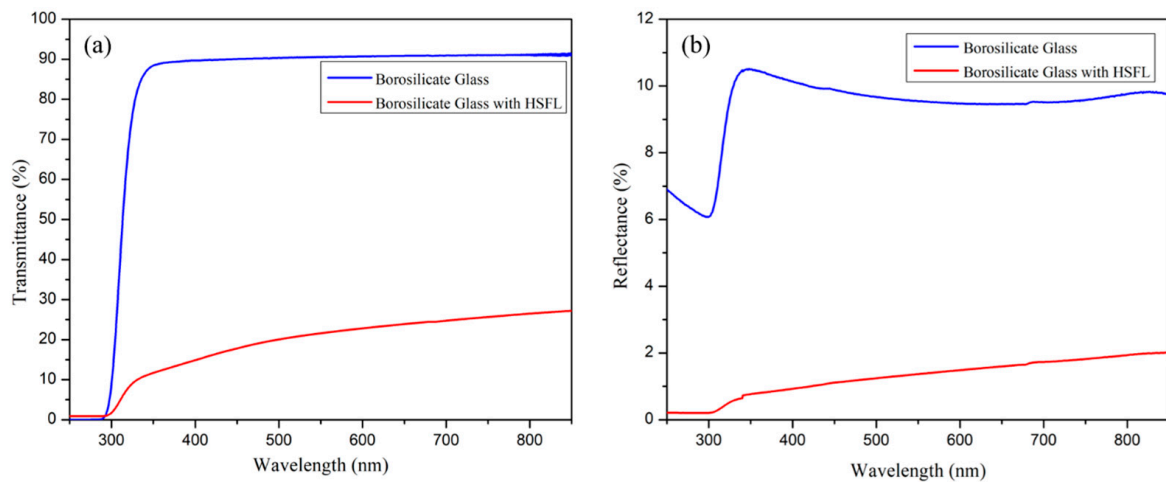


Figure 9. (a) Transmission and (b) reflection spectra of structured borosilicate glass and unstructured borosilicate glass.

The wettability of the structured borosilicate glass was compared with the unstructured borosilicate glass by taking the contact angle measurement (Figure 10a,b). The initial, non-irradiated borosilicate glass surface was characterized by a contact angle of $\theta \approx 42^\circ$, which corresponds to the hydrophilic behavior of the glass surface. After the formation of HSFL, the contact angle was decreased to $\theta \approx 8^\circ$, which corresponds to a superhydrophilic behavior of the surface. This super-hydrophilic behavior of borosilicate glass with HSFL can be explained using Wenzel’s model. This takes into account how the roughness factor r

affects the contact angle of an initially flat surface according to the equation $\cos \theta_w = r \cos \theta$ [61], where the roughness factor r is the ratio of actual surface area to the geometrical surface area. So, according to this relation, the theoretical roughness factor can be estimated as $r = 1.33$. However, from the AFM measurements, the roughness factor can be estimated as $r = 1.35$. This deviation in the roughness factor is due to the fact that the Wenzel model only considers the topographical aspects, whereas Kietzig et al. report that the surface chemistry also has significant effect on wetting properties [62].

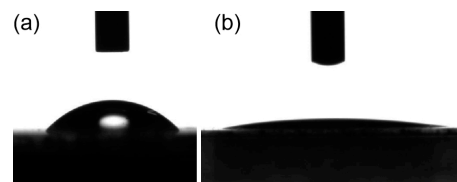


Figure 10. Wettability of (a) unstructured borosilicate glass and (b) structured borosilicate glass.

4. Conclusions

We investigated the generation of high-spatial-frequency laser-induced periodic surface structures (HSFL) on borosilicate glass using femtosecond laser pulses. The effects of laser fluence (F), number of laser shots (N), and scan direction with respect to laser polarization on large-area surface structuring were thoroughly investigated. The single-pulse ablation threshold of borosilicate glass was found to be $3.87 \pm 0.26 \text{ J/cm}^2$, and the incubation factor was found to be 0.68 ± 0.03 . Single-spot experiments showed that the uniform LIPSS formation is limited by melt and crater formation inside the irradiated area for higher fluence and a larger number of irradiated laser pulses. The induced ripple structures were oriented parallel to the electric field vector. The orientation of the scan axis with respect to the laser beam polarization and scan speed were found to significantly affect the uniformity of LIPSS generated along the scan line. More redeposition and melt formation occurred when the scan axis was perpendicular to the laser beam polarization, and the higher scan speeds resulted in structures with a smaller spread of orientation angles. The optimal conditions for large-area processing were found to be a laser peak fluence of 2.71 J/cm^2 and a scan speed of $2000 \text{ } \mu\text{m/s}$. These conditions were used to create large areas of HSFLs with periodicities of approximately 380 nanometers. The processed borosilicate glass surface exhibits iridescence because of the presence of uniform HSFL. The significant decrease in the reflection and transmittance, as well as the change in wettability from hydrophilic to superhydrophilic, demonstrates the potential of using large-area HSFL structures in optics, microfluidics, photovoltaics, and biomaterials.

Author Contributions: Conceptualization, R.R. and K.K.A.; methodology, R.R.; validation, R.R., E.R.K. and K.K.A.; formal analysis, R.R.; investigation, R.R.; resources, R.R. and K.K.A.; data curation, R.R. and E.R.K.; writing—original draft preparation, R.R. and E.R.K.; writing—review and editing, K.K.A.; supervision, K.K.A.; project administration, K.K.A.; funding acquisition, K.K.A. All authors have read and agreed to the published version of the manuscript.

Funding: RR acknowledges the University Grand Commission (UGC), Govt. of India, for Junior Research Fellowship for PhD program [NTA Ref. No.: 191620101085]. This research was supported by the Chancellor's Award Grant (267/2021/HEDN, No.CUSAT/PL(B).A3/1793/2021) from the Government of Kerala.

Data Availability Statement: The data presented in this study are available on request.

Acknowledgments: The research work presented in this paper was supported by the Chancellor's Award Grant (267/2021/HEDN, No. CUSAT/PL(B).A3/1793/2021) from the Government of Kerala. The authors would also like to extend their appreciation to the Inter-University Centre for Nanomaterials and Devices (IUCND) and the Centre of Excellence in Advanced Materials (CAM) for providing the necessary experimental facilities. R. R. acknowledges the valuable assistance of Arun G (Technical Assistant, Department of Physics, CUSAT) and Arun Pappachan (Research Scholar, International

School of Photonics, CUSAT) for their contributions in FESEM and UV-VIS-NIR Spectrophotometer measurements, respectively.

Conflicts of Interest: The authors declare no conflict of interest.

References

1. Bonse, J.; Kirner, S.V.; Höhm, S.; Epperlein, N.; Spaltmann, D.; Rosenfeld, A.; Krüger, J. Applications of Laser-Induced Periodic Surface Structures (LIPSS). In Proceedings of the Laser-Based Micro- and Nanoprocessing XI, San Francisco, CA, USA, 31 January–2 February 2017; Klotzbach, U., Washio, K., Kling, R., Eds.; SPIE: Bellingham, WA, USA, 2017; Volume 10092, p. 100920N.
2. Vorobyev, A.Y.; Guo, C. Direct Femtosecond Laser Surface Nano/Microstructuring and Its Applications. *Laser Photonics Rev.* **2013**, *7*, 385–407. [[CrossRef](#)]
3. Bonse, J.; Koter, R.; Hartelt, M.; Spaltmann, D.; Pentzien, S.; Höhm, S.; Rosenfeld, A.; Krüger, J. Femtosecond Laser-Induced Periodic Surface Structures on Steel and Titanium Alloy for Tribological Applications. *Appl. Phys. A Mater. Sci. Process.* **2014**, *117*, 103–110. [[CrossRef](#)]
4. Yang, J.; Yang, Y.; Zhao, B.; Wang, Y.; Zhu, X. Femtosecond Laser-Induced Surface Structures to Significantly Improve the Thermal Emission of Light from Metals. *Appl. Phys. B* **2012**, *106*, 349–355. [[CrossRef](#)]
5. Shukla, P.; Waugh, D.G.; Lawrence, J.; Vilar, R. 10-Laser Surface Structuring of Ceramics, Metals and Polymers for Biomedical Applications: A Review. In *Laser Surface Modification of Biomaterials*; Vilar, R., Ed.; Woodhead Publishing: Sawston, UK, 2016; pp. 281–299. ISBN 978-0-08-100883-6.
6. Sipe, J.E.; Young, J.F.; Preston, J.S.; van Driel, H.M. Laser-Induced Periodic Surface Structure. I. Theory. *Phys. Rev. B* **1983**, *27*, 1141–1154. [[CrossRef](#)]
7. Bonse, J.; Krüger, J.; Höhm, S.; Rosenfeld, A. Femtosecond Laser-Induced Periodic Surface Structures. *J. Laser Appl.* **2012**, *24*, 042006. [[CrossRef](#)]
8. Nivas, J.J.J.; Amoroso, S. Generation of Supra-Wavelength Grooves in Femtosecond Laser Surface Structuring of Silicon. *Nanomaterials* **2021**, *11*, 174. [[CrossRef](#)]
9. Mastellone, M.; Pace, M.L.; Curcio, M.; Caggiano, N.; De Bonis, A.; Teghil, R.; Dolce, P.; Mollica, D.; Orlando, S.; Santagata, A.; et al. LIPSS Applied to Wide Bandgap Semiconductors and Dielectrics: Assessment and Future Perspectives. *Materials* **2022**, *15*, 1378. [[CrossRef](#)]
10. Zhang, Y.; Jiang, Q.; Long, M.; Han, R.; Cao, K.; Zhang, S.; Feng, D.; Jia, T.; Sun, Z.; Qiu, J.; et al. Femtosecond Laser-Induced Periodic Structures: Mechanisms, Techniques, and Applications. *Opto-Electron. Sci.* **2022**, *1*, 220005. [[CrossRef](#)]
11. Zhang, D.; Li, C.; Xu, J.; Liu, R.; Duan, R.; Feng, K.; Li, Z. Higher Suitability of NbMoTaW over Its Elemental Metals for Laser Induced Periodic Surface Structure/Particle-Aggregate UV-to-MIR Ultrabroadband Absorber. *Scr. Mater.* **2023**, *227*, 115276. [[CrossRef](#)]
12. Bonse, J.; Hohm, S.; Kirner, S.V.; Rosenfeld, A.; Krüger, J. Laser-Induced Periodic Surface Structures—A Scientific Evergreen. *IEEE J. Sel. Top. Quantum Electron.* **2017**, *23*, 109–123. [[CrossRef](#)]
13. Höhm, S.; Rosenfeld, A.; Krüger, J.; Bonse, J. Femtosecond Laser-Induced Periodic Surface Structures on Silica. *J. Appl. Phys.* **2012**, *112*, 014901. [[CrossRef](#)]
14. Reif, J.; Costache, F.; Henyk, M.; Pandelov, S.V. Ripples Revisited: Non-Classical Morphology at the Bottom of Femtosecond Laser Ablation Craters in Transparent Dielectrics. *Appl. Surf. Sci.* **2002**, *197–198*, 891–895. [[CrossRef](#)]
15. Bonse, J.; Krüger, J. Pulse Number Dependence of Laser-Induced Periodic Surface Structures for Femtosecond Laser Irradiation of Silicon. *J. Appl. Phys.* **2010**, *108*, 034903. [[CrossRef](#)]
16. Bonse, J.; Rosenfeld, A.; Krüger, J. On the Role of Surface Plasmon Polaritons in the Formation of Laser-Induced Periodic Surface Structures upon Irradiation of Silicon by Femtosecond-Laser Pulses. *J. Appl. Phys.* **2009**, *106*, 104910. [[CrossRef](#)]
17. Liang, F.; Vallée, R.; Chin, S.L. Mechanism of Nanograting Formation on the Surface of Fused Silica. *Opt. Express* **2012**, *20*, 4389. [[CrossRef](#)]
18. Liao, Y.; Ni, J.; Qiao, L.; Huang, M.; Bellouard, Y.; Sugioka, K.; Cheng, Y. High-Fidelity Visualization of Formation of Volume Nanogratings in Porous Glass by Femtosecond Laser Irradiation. *Optica* **2015**, *2*, 329–334. [[CrossRef](#)]
19. Le Harzic, R.; Dörr, D.; Sauer, D.; Neumeier, M.; Epple, M.; Zimmermann, H.; Stracke, F. Large-Area, Uniform, High-Spatial-Frequency Ripples Generated on Silicon Using a Nanojoule-Femtosecond Laser at High Repetition Rate. *Opt. Lett.* **2011**, *36*, 229–231. [[CrossRef](#)]
20. Dufft, D.; Rosenfeld, A.; Das, S.K.; Grunwald, R.; Bonse, J. Femtosecond Laser-Induced Periodic Surface Structures Revisited: A Comparative Study on ZnO. *J. Appl. Phys.* **2009**, *105*, 034908. [[CrossRef](#)]
21. Jia, T.Q.; Chen, H.X.; Huang, M.; Zhao, F.L.; Qiu, J.R.; Li, R.X.; Xu, Z.Z.; He, X.K.; Zhang, J.; Kuroda, H. Formation of Nanogratings on the Surface of a ZnSe Crystal Irradiated by Femtosecond Laser Pulses. *Phys. Rev. B Condens. Matter Mater. Phys.* **2005**, *72*, 125429. [[CrossRef](#)]
22. Zhang, D.; Ranjan, B.; Tanaka, T.; Sugioka, K. Carbonized Hybrid Micro/Nanostructured Metasurfaces Produced by Femtosecond Laser Ablation in Organic Solvents for Biomimetic Antireflective Surfaces. *ACS Appl. Nano Mater.* **2020**, *3*, 1855–1871. [[CrossRef](#)]

23. Hnatovsky, C.; Taylor, R.S.; Simova, E.; Rajeev, P.P.; Rayner, D.M.; Bhardwaj, V.R.; Corkum, P.B. Fabrication of Microchannels in Glass Using Focused Femtosecond Laser Radiation and Selective Chemical Etching. *Appl. Phys. A Mater. Sci. Process.* **2006**, *84*, 47–61. [[CrossRef](#)]
24. Huang, M.; Zhao, F.; Cheng, Y.; Xu, N.; Xu, Z. Mechanisms of Ultrafast Laser-Induced Deep-Subwavelength Gratings on Graphite and Diamond. *Phys. Rev. B Condens. Matter Mater. Phys.* **2009**, *79*, 125436. [[CrossRef](#)]
25. Das, S.K.; Messaoudi, H.; Debroy, A.; McGlynn, E.; Grunwald, R. Multiphoton Excitation of Surface Plasmon-Polaritons and Scaling of Nanoripple Formation in Large Bandgap Materials. *Opt. Mater. Express* **2013**, *3*, 1705. [[CrossRef](#)]
26. Huang, M.; Zhao, F.; Cheng, Y.; Xu, N.; Xu, Z. Origin of Laser-Induced near-Subwavelength Ripples: Interference between Surface Plasmons and Incident Laser. *ACS Nano* **2009**, *3*, 4062–4070. [[CrossRef](#)] [[PubMed](#)]
27. Borowiec, A.; Haugen, H.K. Subwavelength Ripple Formation on the Surfaces of Compound Semiconductors Irradiated with Femtosecond Laser Pulses. *Appl. Phys. Lett.* **2003**, *82*, 4462–4464. [[CrossRef](#)]
28. Taher, M.A.; Chaudhary, N.; Thirunaukkarasu, K.; Rajput, V.K.; Naraharisetty, S.R.G. Controlled Periodicities of Ladder-like Structures via Femtosecond Laser of Wavelength from 400 Nm to 2200 Nm. *Surf. Interfaces* **2022**, *28*, 101622. [[CrossRef](#)]
29. Maragkaki, S.; Derrien, T.J.Y.; Levy, Y.; Bulgakova, N.M.; Ostendorf, A.; Gurevich, E.L. Wavelength Dependence of Picosecond Laser-Induced Periodic Surface Structures on Copper. *Appl. Surf. Sci.* **2017**, *417*, 88–92. [[CrossRef](#)]
30. Shi, X.; Xu, X. Laser Fluence Dependence of Ripple Formation on Fused Silica by Femtosecond Laser Irradiation. *Appl. Phys. A Mater. Sci. Process.* **2019**, *125*, 256. [[CrossRef](#)]
31. Gregorčič, P.; Sedlaček, M.; Podgornik, B.; Reif, J. Formation of Laser-Induced Periodic Surface Structures (LIPSS) on Tool Steel by Multiple Picosecond Laser Pulses of Different Polarizations. *Appl. Surf. Sci.* **2016**, *387*, 698–706. [[CrossRef](#)]
32. Gräf, S.; Kunz, C.; Engel, S.; Derrien, T.J.Y.; Müller, F.A. Femtosecond Laser-Induced Periodic Surface Structures on Fused Silica: The Impact of the Initial Substrate Temperature. *Materials* **2018**, *11*, 1340. [[CrossRef](#)]
33. Albu, C.; Dinescu, A.; Filipescu, M.; Ulmeanu, M.; Zamfirescu, M. Periodical Structures Induced by Femtosecond Laser on Metals in Air and Liquid Environments. *Appl. Surf. Sci.* **2013**, *278*, 347–351. [[CrossRef](#)]
34. Nürnberger, P.; Reinhardt, H.; Kim, H.C.; Yang, F.; Peppler, K.; Janek, J.; Hampp, N. Influence of Substrate Microcrystallinity on the Orientation of Laser-Induced Periodic Surface Structures. *J. Appl. Phys.* **2015**, *118*, 134306. [[CrossRef](#)]
35. Kunz, C.; Engel, S.; Müller, F.A.; Gräf, S. Large-Area Fabrication of Laser-Induced Periodic Surface Structures on Fused Silica Using Thin Gold Layers. *Nanomaterials* **2020**, *10*, 1187. [[CrossRef](#)] [[PubMed](#)]
36. Choi, J.; Schwarz, C. Advances in Femtosecond Laser Processing of Optical Material for Device Applications. *Int. J. Appl. Glass Sci.* **2020**, *11*, 480–490. [[CrossRef](#)]
37. Xu, S.Z.; Dou, H.Q.; Sun, K.; Ye, Y.Y.; Li, Z.; Wang, H.J.; Liao, W.; Liu, H.; Miao, X.X.; Yuan, X.D.; et al. Scan Speed and Fluence Effects in Femtosecond Laser Induced Micro/Nano-Structures on the Surface of Fused Silica. *J. Non Cryst. Solids* **2018**, *492*, 56–62. [[CrossRef](#)]
38. Schwarz, S.; Rung, S.; Esen, C.; Hellmann, R. Surface Plasmon Polariton Triggered Generation of 1D-Low Spatial Frequency LIPSS on Fused Silica. *Appl. Sci.* **2018**, *8*, 1624. [[CrossRef](#)]
39. Gräf, S.; Kunz, C.; Müller, F.A. Formation and Properties of Laser-Induced Periodic Surface Structures on Different Glasses. *Materials* **2017**, *10*, 933. [[CrossRef](#)]
40. Richter, S.; Miese, C.; Döring, S.; Zimmermann, F.; Withford, M.J.; Tünnermann, A.; Nolte, S. Laser Induced Nanogratings beyond Fused Silica-Periodic Nanostructures in Borosilicate Glasses and ULE™. *Opt. Mater. Express* **2013**, *3*, 1161. [[CrossRef](#)]
41. Liu, J.M. Simple Technique for Measurements of Pulsed Gaussian-Beam Spot Sizes. *Opt. Lett.* **1982**, *7*, 196–198. [[CrossRef](#)]
42. Jee, Y.; Becker, M.F.; Walser, R.M. Laser-Induced Damage on Single-Crystal Metal Surfaces. *J. Opt. Soc. Am. B* **1988**, *5*, 648–659. [[CrossRef](#)]
43. Nečas, D.; Klapetek, P. Gwyddion: An Open-Source Software for SPM Data Analysis. *Open Phys.* **2012**, *10*, 181–188. [[CrossRef](#)]
44. Schindelin, J.; Rueden, C.T.; Hiner, M.C.; Eliceiri, K.W. The ImageJ Ecosystem: An Open Platform for Biomedical Image Analysis. *Mol. Reprod. Dev.* **2015**, *82*, 518–529. [[CrossRef](#)] [[PubMed](#)]
45. Gnilitzky, I.; Derrien, T.J.Y.; Levy, Y.; Bulgakova, N.M.; Mocek, T.; Orazi, L. High-Speed Manufacturing of Highly Regular Femtosecond Laser-Induced Periodic Surface Structures: Physical Origin of Regularity. *Sci. Rep.* **2017**, *7*, 8485. [[CrossRef](#)] [[PubMed](#)]
46. Püspöki, Z.; Storath, M.; Sage, D.; Unser, M. Transforms and Operators for Directional Bioimage Analysis: A Survey. In *Focus on Bio-Image Informatics*; De Vos Winnok, H., Munck, S., Timmermans, J.-P., Eds.; Springer International Publishing: Cham, Switzerland, 2016; pp. 69–93. ISBN 978-3-319-28549-8.
47. Raciukaitis, G.; Brikas, M.; Gecys, P.; Gedvilas, M. Accumulation Effects in Laser Ablation of Metals with High-Repetition-Rate Lasers. In Proceedings of the High-Power Laser Ablation VII, Taos, NM, USA, 8 May 2008; SPIE: Taos, NM, USA, 2008; Volume 7005, p. 70052L.
48. Bonse, J.; Sturm, H.; Schmidt, D.; Kautek, W. Chemical, Morphological and Accumulation Phenomena in Ultrashort-Pulse Laser Ablation of TiN in Air. *Appl. Phys. A Mater. Sci. Process.* **2000**, *71*, 657–665. [[CrossRef](#)]
49. Di Niso, F.; Gaudiuso, C.; Sibillano, T.; Mezzapesa, F.P.; Ancona, A.; Lugarà, P.M. Role of Heat Accumulation on the Incubation Effect in Multi-Shot Laser Ablation of Stainless Steel at High Repetition Rates. *Opt. Express* **2014**, *22*, 12200. [[CrossRef](#)]
50. Ben-Yakar, A.; Byer, R.L. Femtosecond Laser Ablation Properties of Borosilicate Glass. *J. Appl. Phys.* **2004**, *96*, 5316–5323. [[CrossRef](#)]

51. Mannion, P.T.; Magee, J.; Coyne, E.; O'Connor, G.M.; Glynn, T.J. The Effect of Damage Accumulation Behaviour on Ablation Thresholds and Damage Morphology in Ultrafast Laser Micro-Machining of Common Metals in Air. *Appl. Surf. Sci.* **2004**, *233*, 275–287. [[CrossRef](#)]
52. Neuenschwander, B.; Jaeggi, B.; Schmid, M.; Dommann, A.; Neels, A.; Bandi, T.; Hennig, G. Factors Controlling the Incubation in the Application of Ps Laser Pulses on Copper and Iron Surfaces. In Proceedings of the Laser Applications in Microelectronic and Optoelectronic Manufacturing (LAMOM) XVIII, San Francisco, CA, USA, 4–7 February 2013; Xu, X., Hennig, G., Nakata, Y., Roth, S.W., Eds.; SPIE: Taos, NM, USA, 2013; Volume 8607, p. 86070D.
53. Ben-Yakar, A.; Harkin, A.; Ashmore, J.; Byer, R.L.; Stone, H.A. Thermal and Fluid Processes of a Thin Melt Zone during Femtosecond Laser Ablation of Glass: The Formation of Rims by Single Laser Pulses. *J. Phys. D Appl. Phys.* **2007**, *40*, 1447–1459. [[CrossRef](#)]
54. Laville, S.; Vidal, F.; Johnston, T.W.; Chaker, M.; Le Drogoff, B.; Barthélemy, O.; Margot, J.; Sabsabi, M. Modeling the Time Evolution of Laser-Induced Plasmas for Various Pulse Durations and Fluences. *Phys. Plasmas* **2004**, *11*, 2182–2190. [[CrossRef](#)]
55. Ben-Yakar, A.; Byer, R.L.; Harkin, A.; Ashmore, J.; Stone, H.A.; Shen, M.; Mazur, E. Morphology of Femtosecond-Laser-Ablated Borosilicate Glass Surfaces. *Appl. Phys. Lett.* **2003**, *83*, 3030–3032. [[CrossRef](#)]
56. Mastellone, M.; Bellucci, A.; Girolami, M.; Serpente, V.; Polini, R.; Orlando, S.; Santagata, A.; Sani, E.; Hitzel, F.; Trucchi, D.M. Deep-Subwavelength 2D Periodic Surface Nanostructures on Diamond by Double-Pulse Femtosecond Laser Irradiation. *Nano Lett.* **2021**, *21*, 4477–4483. [[CrossRef](#)] [[PubMed](#)]
57. Wang, H.; Zhang, F.; Yin, K.; Duan, J. Bioinspired Antireflective Subwavelength Nanostructures Induced by Femtosecond Laser for High Transparency Glass. *J. Non Cryst. Solids* **2023**, *600*, 122016. [[CrossRef](#)]
58. Raguin, D.H.; Morris, G.M. Antireflection Structured Surfaces for the Infrared Spectral Region. *Appl. Opt.* **1993**, *32*, 1154–1167. [[CrossRef](#)] [[PubMed](#)]
59. Grann, E.B.; Moharam, M.G.; Pommet, D.A. Optimal Design for Antireflective Tapered Two-Dimensional Subwavelength Grating Structures. *J. Opt. Soc. Am. A* **1995**, *12*, 333–339. [[CrossRef](#)]
60. Yilbas, B.S.; Khaled, M.; Abu-Dheir, N.; Al-Aqeeli, N.; Said, S.A.M.; Ahmed, A.O.M.; Varanasi, K.K.; Toumi, Y.K. Wetting and Other Physical Characteristics of Polycarbonate Surface Textured Using Laser Ablation. *Appl. Surf. Sci.* **2014**, *320*, 21–29. [[CrossRef](#)]
61. Wenzel, R.N. RESISTANCE OF SOLID SURFACES TO WETTING BY WATER. *Ind. Eng. Chem.* **1936**, *28*, 988–994. [[CrossRef](#)]
62. Kietzig, A.M.; Hatzikiriakos, S.G.; Englezos, P. Patterned Superhydrophobic Metallic Surfaces. *Langmuir* **2009**, *25*, 4821–4827. [[CrossRef](#)]

Disclaimer/Publisher's Note: The statements, opinions and data contained in all publications are solely those of the individual author(s) and contributor(s) and not of MDPI and/or the editor(s). MDPI and/or the editor(s) disclaim responsibility for any injury to people or property resulting from any ideas, methods, instructions or products referred to in the content.